Symmetric Factorization of the Conformation Tensor in Viscoelastic Fluid Models

Nusret Balci
University of Minnesota Twin Cities

Becca Thomases
University of Minnesota Twin Cities, bthomases@smith.edu

Michael Renardy
University of Minnesota Twin Cities

Charles R. Doering
University of Minnesota Twin Cities

Recommended Citation

Symmetric factorization of the conformation tensor in viscoelastic fluid models

Nusret Balci [a], Becca Thomases [a,b], Michael Renardy [a,c], Charles R. Doering [a,d,e,f,*]

[a] Institute for Mathematics and its Applications, University of Minnesota, Minneapolis, MN 55455-0134, United States
[b] Department of Mathematics, University of California, Davis, CA 95616, United States
[c] Department of Mathematics, Virginia Tech, Blacksburg, VA 24061-0123, United States
[d] Department of Physics, University of Michigan, Ann Arbor, MI 48109-1040, United States
[e] Department of Mathematics, University of Michigan, Ann Arbor, MI 48109-1043, United States
[f] Center for the Study of Complex Systems, University of Michigan, Ann Arbor, MI 48109-1107, United States

ARTICLE INFO

ABSTRACT

The positive-definite symmetric polymer conformation tensor possesses a unique symmetric square root that satisfies a closed evolution equation in the Oldroyd-B and FENE-P models of viscoelastic fluid flow. When expressed in terms of the velocity field and the symmetric square root of the conformation tensor, these models' equations of motion formally constitute an evolution in a Hilbert space with a total energy functional that defines a norm. Moreover, this formulation is easily implemented in direct numerical simulations resulting in significant practical advantages in terms of both accuracy and stability.

© 2011 Elsevier B.V. All rights reserved.

1. Introduction

Familiar models of viscoelastic polymeric fluids present challenging problems for both mathematical analysis and numerical computations. One of the difficulties stems from the nature of the stress evolution equations. Although there is indeed some stress diffusion, the diffusion of polymers is typically orders of magnitude smaller than that for non-polymeric molecules and so is often neglected in direct numerical simulations. The difficulties manifest themselves both in the form of loss of accuracy and stability in numerical schemes, and in the absence of effective *a priori* estimates for analysis. Despite recent progress in the field, many important problems remain open.

In this paper we focus on two models, Oldroyd-B and FENE-P. It has proven to be a difficult task to devise numerical schemes that are efficient, accurate, and stable at the same time. One way to ease the numerical problems is to add artificially large stress diffusion, and this has been done for a long time. Fattal and Kupferman [1] proposed a log-conformation scheme directly evolving the matrix logarithm of the positive definite conformation tensor that, according to their reports, indeed helps with stability issues.

Another method developed by Collins and co-workers [2] evolves the eigenvalues of the conformation tensor. Lozinski and Owens [3] also proposed to work with the deformation tensor, another of the square roots of the conformation tensor.

We consider a square root method as well, but unlike any previous work we are aware of, we derive an evolution equation for the positive-definite square square root by taking advantage of the $O(n)$ degeneracy in the matrix square root in n dimensions. This turns out to be both theoretically and numerically convenient. On the one hand it allows the dependent variables in the Oldroyd-B and FENE-P models to take values in a vector space with a natural norm defined by the physical energy. On the other hand we observe that, at practically no additional computational cost, this formulation produces significant gains in both numerical stability and numerical accuracy—without adding any artificial stress diffusion—as compared to directly evolving the conformation tensor. We note in particular that the flow studied in this paper has a hyperbolic stagnation point and our simulations for the Oldroyd-B model extend far beyond the Weissenberg number at which the stress in the associated steady flow becomes infinite.

2. Mathematical framework

The nondimensional equations of motion are

$$\frac{\partial \mathbf{u}(\mathbf{x}, t)}{\partial t} + \mathbf{u} \cdot \nabla \mathbf{u} + \nabla p = \frac{1}{Re} \Delta \mathbf{u} + \nabla \cdot \boldsymbol{\tau} + \mathbf{f}(\mathbf{x}, t), \quad \nabla \cdot \mathbf{u} = 0, \quad (1)$$

* Corresponding author at: Department of Mathematics, University of Michigan, Ann Arbor, MI 48109-1043, United States.
E-mail address: doering@umich.edu (C.R. Doering).

with $\mathbf{x} \in \mathcal{R}^n$ ($n = 2$ or 3) and Reynolds number $Re = U\ell/\nu$ where U and ℓ represent appropriate choices of velocity and length scales for the problem under investigation. The externally applied body force is denoted by $\mathbf{f}$, and the polymer stress tensor $\boldsymbol{\tau}(\mathbf{x}, t)$ is

$$\boldsymbol{\tau} = -\frac{s}{Re}\,\mathbf{s}(\mathbf{c}) \tag{2}$$

where the symmetric positive-definite polymer conformation (a.k.a. configuration) tensor $\mathbf{c}(\mathbf{x}, t)$ evolves according to

$$\frac{\partial \mathbf{c}}{\partial t} + \mathbf{u} \cdot \nabla \mathbf{c} = \mathbf{c}\nabla \mathbf{u} + (\nabla \mathbf{u})^T \mathbf{c} + \mathbf{s}(\mathbf{c}). \tag{3}$$

The parameter s is a coupling constant proportional to the concentration of the polymers in the fluid, and the tensor $\mathbf{s}(\mathbf{c})$ takes different forms in various non-Newtonian models. For the Oldroyd-B model

$$\mathbf{s}(\mathbf{c}) = \frac{1}{Wi}(\mathbf{I} - \mathbf{c}) \tag{4}$$

where the Weissenberg number $Wi = U\lambda/\ell$ is the product of the polymer relaxation time λ and the rate of strain U/ℓ. For the FENE-P model

$$\mathbf{s}(\mathbf{c}) = \frac{1}{Wi}\left(\mathbf{I} - \frac{\mathbf{c}}{1 - (tr\mathbf{c}/l^2)}\right), \tag{5}$$

where l^2 is proportional to the square of the maximum polymer length. For both models the total mechanical energy of the system is the sum of the fluid's kinetic energy and the elastic potential energy of the polymers:

$$\mathcal{E}(t) = \frac{1}{2}\int \left[|\mathbf{u}(\mathbf{x}, t)|^2 + tr\,\boldsymbol{\tau}\right]\,dx\,dy\,dz. \tag{6}$$

This energy[1] is formally conserved by the dynamics in the limits of infinite Reynolds and Weissenberg numbers.

Unlike the situation for Newtonian fluids modeled by the incompressible Navier–Stokes (or Stokes) equations, the total energy does not define a natural norm, or even a metric, in the phase space of the dynamical fields $\mathbf{u}$ and $\mathbf{c}$. Indeed, the $(\mathbf{u}, \mathbf{c})$ phase space is not even a linear vector space. This mathematical awkwardness results from the fact that a linear combination of positive matrices is not necessarily positive. And even if we extend consideration to all symmetric matrices, then the trace is not always positive. This circumstance complicates analysis of these models and precludes implementation of useful techniques including nonlinear (energy) stability notions [4].

This problem can be circumvented, however, by reformulating the models in terms of the (unique) positive symmetric square root $\mathbf{b}(\mathbf{x}, t)$ of the conformation tensor $\mathbf{c}(\mathbf{x}, t)$. We write

$$c_{ij}(\mathbf{x}, t) = \sum_{k=1}^{n} b_{ik}(\mathbf{x}, t)b_{kj}(\mathbf{x}, t) \quad \text{with} \quad b_{ij}(\mathbf{x}, t) = b_{ji}(\mathbf{x}, t), \tag{7}$$

so the polymer energy density is a quadratic function of the matrix (Frobenius) norm of $\mathbf{b}$,

$$\|\mathbf{b}\|^2 = \sum_{i,j=1}^{n} b_{ij}^2 = tr(\mathbf{b}^T\mathbf{b}) = tr\,\mathbf{c}. \tag{8}$$

The work required to implement this proposal is to precisely articulate the dynamics of $\mathbf{b}$, a not altogether trivial task due to the inherent degeneracy of the matrix square root.

In the Oldroyd-B case solutions of differential equations of the form

$$\left(\frac{\partial}{\partial t} + \mathbf{u} \cdot \nabla\right)\mathbf{b} = \mathbf{b}\nabla\mathbf{u} + \mathbf{a}\mathbf{b} + \frac{1}{2Wi}((\mathbf{b}^T)^{-1} - \mathbf{b}), \tag{9}$$

where $\mathbf{a}(\mathbf{x}, t)$ is *any* antisymmetric matrix, satisfy $\mathbf{b}^T\mathbf{b} = \mathbf{c}$ pointwise in space and time when the initial data satisfy $\mathbf{b}^T(\mathbf{x}, 0)\mathbf{b}(\mathbf{x}, 0) = \mathbf{c}(\mathbf{x}, 0)$. Likewise, in the FENE-P case the evolution

$$\left(\frac{\partial}{\partial t} + \mathbf{u} \cdot \nabla\right)\mathbf{b} = \mathbf{b}\nabla\mathbf{u} + \mathbf{a}\mathbf{b} + \frac{1}{2Wi}\left((\mathbf{b}^T)^{-1} - \frac{\mathbf{b}}{1 - \|\mathbf{b}\|^2/l^2}\right), \tag{10}$$

produces such a square root of $\mathbf{c}$ when $\mathbf{a}(\mathbf{x}, t)$ is any antisymmetric matrix and $\mathbf{b}^T(\mathbf{x}, 0)\mathbf{b}(\mathbf{x}, 0) = \mathbf{c}(\mathbf{x}, 0)$. The key observation is that by choosing $\mathbf{a}(\mathbf{x}, t)$ properly we can tune the evolution Eqs. (9) and (10)—and similar models with an upper convective derivative—to preserve the symmetry of $\mathbf{b}$. That is, starting with symmetric initial data $\mathbf{b}^T(\mathbf{x}, 0) = \mathbf{b}(\mathbf{x}, 0)$, the subsequent evolution will preserve the symmetry.

The (i, j)th entry of $\nabla\mathbf{u}$ is denoted by $u_{j,i} = \partial u_j/\partial x_i$, $i, j = 1, 2, 3$ and

$$\mathbf{a} = \begin{pmatrix} 0 & a_{12} & a_{13} \\ -a_{12} & 0 & a_{23} \\ -a_{13} & -a_{23} & 0 \end{pmatrix}, \tag{11}$$

in $n = 3$ spatial dimensions and

$$\mathbf{a} = \begin{pmatrix} 0 & a_{12} \\ -a_{12} & 0 \end{pmatrix} \tag{12}$$

in $n = 2$ dimensions. Define

$$\mathbf{r} = (r_{ij}) = \mathbf{b}(\nabla\mathbf{u}) + \mathbf{a}\mathbf{b}. \tag{13}$$

We now show that we may choose the matrices $\mathbf{a}$, depending on $\nabla\mathbf{u}$ and the symmetric matrix $\mathbf{b}$ pointwise in space and time, so that $\mathbf{r}$ is a field of symmetric matrices, i.e., $r_{ij} = r_{ji}$. For $n = 3$ the explicit formulas for the elements a_{ij} come from solving the system of 3 linear equations

$$(b_{11} + b_{22})a_{12} + b_{23}a_{13} - b_{31}a_{23} = w_1, \tag{14}$$

$$b_{23}a_{12} + (b_{11} + b_{33})a_{13} + b_{12}a_{23} = w_2, \tag{15}$$

$$-b_{13}a_{12} + b_{12}a_{13} + (b_{22} + b_{33})a_{23} = w_3, \tag{16}$$

where

$$w_1 = (b_{12}u_{1,1} - b_{11}u_{2,1}) + (b_{22}u_{1,2} - b_{12}u_{2,2}) + (b_{23}u_{1,3} - b_{13}u_{2,3}), \tag{17}$$

$$w_2 = (b_{13}u_{1,1} - b_{11}u_{3,1}) + (b_{33}u_{1,3} - b_{13}u_{3,3}) + (b_{23}u_{1,2} - b_{12}u_{3,2}), \tag{18}$$

$$w_3 = (b_{13}u_{2,1} - b_{12}u_{3,1}) + (b_{23}u_{2,2} - b_{22}u_{3,2}) + (b_{33}u_{2,3} - b_{23}u_{3,3}). \tag{19}$$

In matrix notation, this is the system of equations

$$\begin{pmatrix} b_{11} + b_{22} & b_{23} & -b_{13} \\ b_{23} & b_{11} + b_{33} & b_{12} \\ -b_{13} & b_{12} & b_{22} + b_{33} \end{pmatrix}\begin{pmatrix} a_{12} \\ a_{13} \\ a_{23} \end{pmatrix} = \begin{pmatrix} w_1 \\ w_2 \\ w_3 \end{pmatrix}. \tag{20}$$

Then by swapping the first and the third columns of the coefficient matrix (and hence, also a_{23} and a_{12}), and subsequently swapping the first and the third rows of the resulting coefficient matrix (and hence, also w_1 and w_3), and finally multiplying the second row and the second column of the resulting matrix by -1 (and hence, also replacing a_{13} and w_2 by $-a_{13}$ and $-w_2$, respectively), we obtain

$$(tr(\mathbf{b})\mathbf{I} - \mathbf{b})\,\tilde{\mathbf{a}} = \mathbf{v}, \tag{21}$$

where

$$\tilde{\mathbf{a}} = \begin{pmatrix} a_{23} \\ -a_{13} \\ a_{12} \end{pmatrix}, \quad \mathbf{v} = \begin{pmatrix} w_3 \\ -w_2 \\ w_1 \end{pmatrix}. \tag{22}$$

---

[1] $\mathcal{E}$ does not include the entropic term that contributes to the free energy of the system.

When $\mathbf{b}$ is symmetric at the point $(\mathbf{x}, t)$ there is an orthogonal matrix $\mathbf{p}(\mathbf{x}, t)$ such that

$$\mathbf{b} = \mathbf{p}^T \text{diag}\left\{\lambda_1, \lambda_2, \lambda_3\right\}\mathbf{p}, \tag{23}$$

where λ_i are the eigenvalues of $\mathbf{b}$. Thus, we have

$$\text{trace}(\mathbf{b})\mathbf{I} - \mathbf{b} = \text{trace}(\mathbf{b})\mathbf{I} - \mathbf{p}^T\text{diag}\left\{\lambda_1, \lambda_2, \lambda_3\right\}\mathbf{p} \tag{24}$$

$$= \mathbf{p}^T(\text{trace}(\mathbf{b})\mathbf{I} - \text{diag}\left\{\lambda_1, \lambda_2, \lambda_3\right\})\mathbf{p} \tag{25}$$

$$= \mathbf{p}^T\text{diag}\left\{\lambda_2 + \lambda_3, \lambda_1 + \lambda_3, \lambda_1 + \lambda_2\right\}\mathbf{p} \tag{26}$$

Again, assuming that $\mathbf{b}$ is positive-definite (although this condition can be clearly relaxed to include a large class of semidefinite objects) we can solve for $\mathbf{a}$ uniquely so that the evolution Eqs. (9) and (10) used to obtain $\mathbf{b}$ at later times are symmetrized. The explicit algebraic formulae for the elements a_{ij} for $n = 3$ are displayed in Appendix A. In the much simpler case of $n = 2$ space dimensions we have

$$a_{12} = \frac{(b_{12}u_{1,1} - b_{11}u_{2,1}) + (b_{22}u_{1,2} - b_{12}u_{2,2})}{b_{11} + b_{22}}. \tag{27}$$

This construction places the full dynamics back in a vector space, namely the direct product of vector fields $\mathbf{u}$ and symmetric tensor fields $\mathbf{b}$. For Oldroyd-B the energy functional (6) is proportional to the vector norm (squared) on the direct product space (modulo an additive constant). For the FENE-P model, the convexity of $\mathbf{b}^2/(1 - \text{tr}\,\mathbf{b}^2/l^2)$ in a neighborhood of the origin, i.e., for $\|\mathbf{b}\| < l$, allows as well for a natural energy norm. And as shown in the next section, in some cases this reformulation of the dynamics leads to significant practical improvements in direct numerical simulations.

3. Numerical experiments

As a test of the numerical accuracy and stability of the square-root method we consider the zero-Reynolds number (Stokes) limit of the Oldroyd-B and FENE-P models in which case the momentum Eq. (1) reduces to

$$\nabla p = \Delta \mathbf{u} + \nabla \cdot \boldsymbol{\tau} + \mathbf{f}, \quad \nabla \cdot \mathbf{u} = 0. \tag{28}$$

Here $\tau = -s\mathbf{s}(\mathbf{c})$ with $\mathbf{s}(\mathbf{c})$ given by (4) or (5) for the Oldroyd-B model or FENE-P model respectively. In the following we fix $s = 0.5$. Following recent studies [5,6] we consider a 2π − periodic domain in $n = 2$ space dimensions ($[-\pi, \pi]^2$) and impose a steady background force

$$\mathbf{f} = (-2\sin x\cos y, 2\cos x\sin y), \tag{29}$$

curl $\mathbf{f}$ is shown in Fig. 1(a). In the absence of polymer stress this yields a four-roll mill geometry for the fluid velocity. One well-known consequence of this body-force imposed extensional geometry in the Oldroyd-B model is that the polymer stress and stress gradients grow exponentially in time [5,7,8] and inevitably produce numerical problems. In particular, when resolving steep gradients the loss of positive-definiteness of the conformation tensor due to numerical error can lead to breakdown of the computational schemes. One common solution to these difficulties is the addition of artificial polymer stress diffusion. Although some polymer stress diffusion can be derived from the basic physics in the model, the magnitude of the physically relevant diffusion is far too small to have an effect on numerical simulations [9]. In the following we do not add *any* stress diffusion to the numerical calculations.

The Stokes–Oldroyd-B system (and FENE-P) is solved with a pseudo-spectral method [10]. The initial data is prescribed for the conformation tensor (or the square-root), and given $\mathbf{c}$ (or $\mathbf{b}$) the Stokes equation is inverted in Fourier space for $\mathbf{u}$. Given $\mathbf{u}$, the nonlinearities of the conformation tensor evolution are evaluated
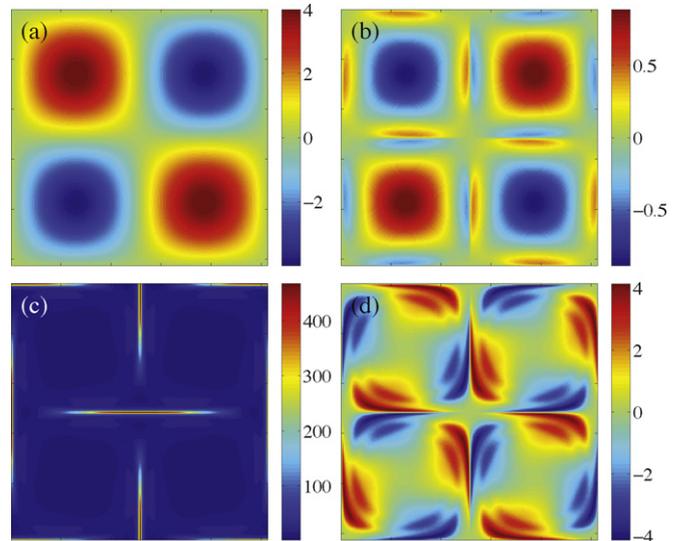

Fig. 1. (a) Contour plots of curl $\mathbf{f}$ for the force given by Eq. (29). (b)–(d) Contour plot of vorticity, tr$\mathbf{c}$, and $\mathbf{c}_{12}$ for isotropic initial data, Wi = 5 at $t = 10$.

using a smooth filter applied in Fourier space before the quadratic terms are multiplied in real space [11]. The conformation tensor is then discretized on the Fourier transform side and is evolved using a second-order Adams-Bashforth method. The method described above is the same method employed in [5] and due to the structural similarity of the evolution of the conformation tensor and the evolution of the square-root it is employed in the same way for both Eqs. (3) and (9). In particular for Eq. (9), the smooth filter is applied to the quadratic terms and cubic terms in Fourier space before these terms are multiplied in real space. Applying a smooth filter is a modification of the 2/3-dealiasing used commonly in spectral methods and has been shown to create fewer oscillations in solutions [11]. It should be noted that due to the explicit formula available the numerical implementation of the square-root method adds no significant computational cost.

In a recent investigation [5] the Stokes–Oldroyd-B equations were solved starting from homogeneous and isotropic initial data, i.e., $\mathbf{c}(0) = \mathbf{I}$, and the stress was observed to diverge (exponentially in time) at the extensional stagnation points in the flow for sufficiently large Weissenberg number. However, outside of an exponentially decreasing region around the extensional stagnation point, the solutions became steady after an initial transient. These near-steady solutions preserve many symmetries: the stress is symmetric and aligned along the direction of extension and the flow has an underlying four-roll structure. For sufficiently large Wi additional oppositely signed vortices arise along the stable and unstable manifolds of the extensional stagnation point. Fig. 1(b)–(d) displays these symmetric solutions in the case Wi = 5, at $t = 10$. These symmetries are broken as the initial data is perturbed and it was shown that instabilities arise for sufficiently large Wi [6,12].

In what follows we discuss both accuracy and stability improvements for the Oldroyd-B and FENE-P models using the square root method. In Section 3.1 we consider homogeneous isotropic initial data $\mathbf{b}(\mathbf{x}, 0) = \mathbf{I}$ and compare solutions to the Stokes–Oldroyd-B model obtained using the direct evolution of $\mathbf{c}$ with those obtained by evolving the symmetric square root. In Subsection 3.2 we consider perturbations to the initial data for the Stokes–Oldroyd-B model (as in previous studies [6,12]) to see how far the simulations run, for a fixed resolution using each method, before numerical divergences appear. Finally, in Section 3.3 we revisit both of these questions for the FENE-P model.
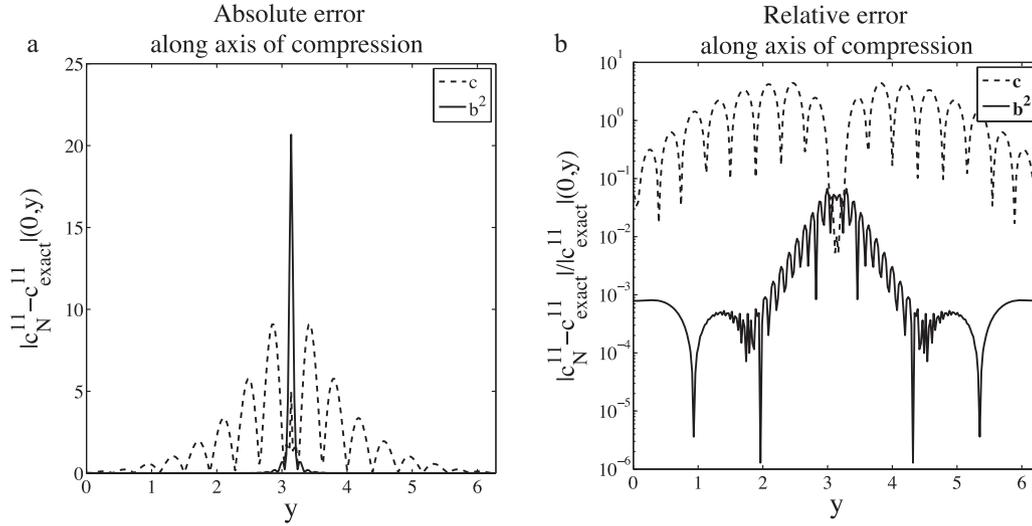
Fig. 2. (a) Absolute error $|\mathbf{c}_N - \mathbf{c}_{\text{exact}}|$ measured along the axis of compression of the first component of the conformation tensor with $N^2 = 256^2$, Wi = 5, at $t = 10$. Dotted line is $\mathbf{c}$ and solid line is $\mathbf{b}^2$. (b) Relative error $|\mathbf{c}_N - \mathbf{c}_{\text{exact}}|/|c_{\text{exact}}|$.

3.1. Accuracy

Fig. 2 shows the difference between the solution to Stokes–Oldroyd-B with $N^2 = 256^2$ grid cells and the "exact" solution computed by evolving $\mathbf{c}$ with $N^2 = 2048^2$ grid cells, resolved to at least 6 digits of accuracy. The dotted line shows the solution computed by directly evolving the conformation tensor $\mathbf{c}$, while the solid line shows the solution computed by evolving the symmetric square root. The simulation is performed with Wi = 5 and the result of the computation is shown at $t = 10$. Panel (a) shows the absolute error ($|\mathbf{c}_N - \mathbf{c}_{\text{exact}}|$) in the first component of the conformation tensor ($\mathbf{c}_{11}$) along the direction of compression because this is precisely where steep gradients form. We observe that away from the extensional stagnation point the square root gives a much better approximation and it is only very near the extensional stagnation point where the evolution of $\mathbf{c}$ gives a better approximation. The relative error is shown in panel (b) to emphasize that although the square-root method's error at the extensional stagnation point is larger, the relative error is actually quite small because the stress is very large there.

Fig. 3 (a) shows the relative error

$$\frac{\|\mathbf{c}_N - \mathbf{c}_{\text{exact}}\|_{L^1}}{\|\mathbf{c}_{\text{exact}}\|_{L^1}} \tag{30}$$

measured in the $L^1([-\pi, \pi]^2)$ norm for both $\mathbf{c}_N$ and $(\mathbf{b}^2)_N$ for $N^2 = 32^2, 64^2, 128^2, 256^2, 512^2$, comparing to the "exact" solution defined by the $N^2 = 2048^2$ simulation. The L^1 norm is chosen because it takes into account the average error over the entire domain. This computation is also for Wi = 5 at $t = 10$.

In this averaged sense we see that the error is always smaller using the square root method. The improvement in accuracy (in the L^1−sense) using the square root method is shown in Fig. 3 (b). Here we plot

$$\frac{|\text{error}_{\mathbf{c}} - \text{error}_{\mathbf{b}^2}|}{|\text{error}_{\mathbf{c}}|} \tag{31}$$

for Wi = 1, 2, 3, 4, 5 for $N^2 = 32^2, 64^2, 128^2, 256^2, 512^2$. Each simulation is computed at $T = t/\text{Wi} = 2$, and this scaled-time is used because the solutions grow exponentially like $e^{t/\text{Wi}}$. There is a significant improvement for higher Wi, in particular for lower resolutions $N^2 = 128^2$ and 256^2.

3.2. Stability

Experiments on low-Reynolds number viscoelastic turbulence [13–15] and instabilities in extensional geometries [16] have inspired many numerical studies of low-Reynolds number viscoelastic fluids [17–19,6,12]. Two main instabilities were observed in one investigation [6,12]: first, for sufficiently large Wi, if a small perturbation is introduced in the initial conformation the extensional stagnation point in the flow becomes unstable and loses the pinning to the background steady force. For larger Wi other stagnation points lose their pinning to the background force and higher oscillations arise in the flow. These instabilities occur on long time scales and some artificial polymer stress diffusion was introduced to fully resolve the stress [6,12]. Here we test these same perturbations to the initial data and for a fixed resolution $N^2 = 256^2$ and run the same simulations *without* any artificial polymer stress diffusion.

Fig. 4 (a) shows a plot of the first component of the conformation tensor for Wi = 10 at $t = 15$ computed both by evolving the conformation tensor (solid line) and the square root (dotted line). The plot is shown along the axis of compression and it is evident that the stress has accumulated significantly and is quite large near the extensional stagnation point in the flow ($y = 0$). The oscillations produced in the direct evolution of $\mathbf{c}$ lead to the loss of positive-definiteness of the conformation tensor, and the numerical scheme breaks down. This figure shown is at $t = 15$ and the computation fails to produce finite numbers at $t = 20$. However using the square root one can run these simulations to $t = 1500$ and even beyond. Fig. 4 (b) shows a plot of max ($\text{tr}(\mathbf{b}^2)$) as a function of time for $0 < t < 1500$. It is important to point out that although max ($\text{tr}(\mathbf{b}^2)$) remains bounded in this case (with *no* artifical stress diffusion) this quantity clearly depends on N and this is one way that the accuracy of the solution is lost. However, it is not clear that this level of loss of accuracy is entirely relevant to the flow because the region where $\text{tr}(\mathbf{b}^2)$ gets large diminishes exponentially in time even as $\text{tr}(\mathbf{b}^2)$ grows exponentially in time [5]. Fig. 4 (c) and (d) show contour plots of $\text{tr}(\mathbf{b}^2)$ and the vorticity of the flow on $[-\pi, \pi]^2$. Here we see that the previously observed instabilities [6,12] are at least qualitatively reproduced. The time-dependent behavior is similar, too: the four-roll mill structure of the background force is preserved initially, the extensional stagnation point leaves the origin, and eventually time-dependent oscillations arise in the flow.
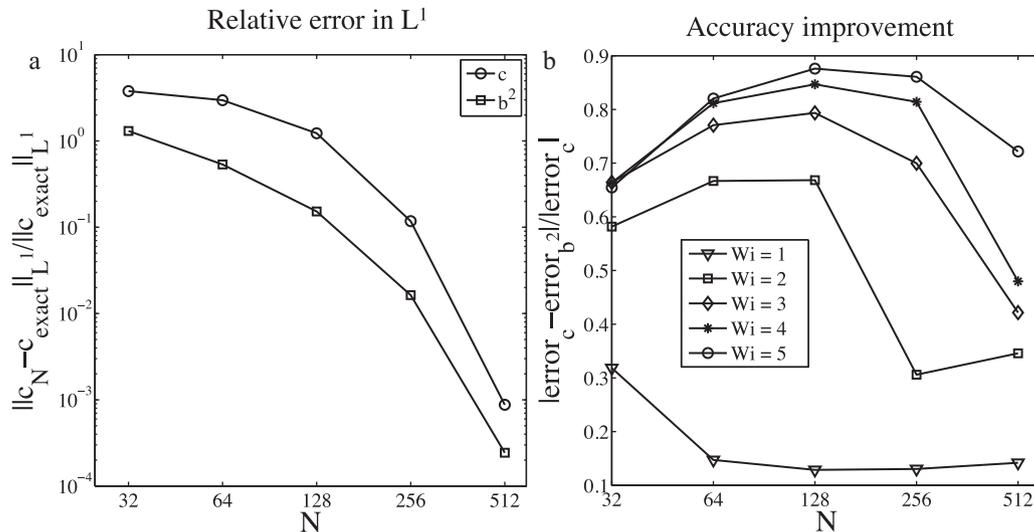
Fig. 3. (a) Relative error in L^1 shows $\|\mathbf{c}_N - \mathbf{c}_{exact}\|_{L^1} / \|\mathbf{c}_{exact}\|_{L^1}$ computed with $\mathbf{c}$ and $\mathbf{b}^2$, for Wi = 5 at t = 10. (b) Improvement in accuracy as a function of N, for Wi = 1 − 5 at $T = t/\mathrm{Wi} = 2$.

Of course with fixed resolution and no stress diffusion there is an inevitable loss of accuracy. This can be seen in Fig. 4 (c) and (d) in the slightly fuzzy images indicating oscillations while attempting to resolve the steep gradients in the conformation tensor and vorticity. It is noteworthy that these simulations are performed with no artificial stress diffusion but nevertheless qualitatively reproduce the well-resolved results that utilized artificial diffusion [6,12]. The same computations simply cannot be performed with a direct evolution of the conformation tensor (in this particular code). The square root method allows simulations to run much longer and at much higher Weissenberg number than evolving $\mathbf{c}$ directly allows. This indicates that it might be possible to use much smaller—closer to the physically realistic quantity—stress diffusion and still obtain reasonably accurate results, although this will not be pursued in this paper.

3.3. FENE-P

The FENE-P model enforces a limit (l^2) on the magnitude of tr $\mathbf{c}$ so the conformation tensor remains bounded. Steep gradients can still arise in the polymer stress, however, and numerical difficulties remain. Therefore we also simulated the FENE-P model in a Stokesian solvent to check for possible accuracy and stability improvements by evolving the symmetric square root.

Fig. 5 (a) and (b) are analogs of Figs. 2 (b) and 3 (a) for FENE-P. The simulations were performed with Wi = 5 and cut-off l^2 = 100, and are displayed at t = 10. Rather than plot the conformation tensor $\mathbf{c}$ and $\mathbf{b}^2$, however, it is more analogous to plot $\mathbf{S} = \mathbf{c}/[1 - (\mathrm{tr}\mathbf{c}/l^2)]$ because this is closely related to the physical stress tensor and includes the factor that gets very large as tr$\mathbf{c}$ gets near the cut-off l^2. The accuracy improvement is not as large here as it was for Oldroyd-B: for Wi = 5 the improvement is about 65% at $N = 256^2$ and is only 31% for $N^2 = 512^2$ but there is still some improvement (especially away from the extensional stagnation point). As before, the "exact" solution here comes from a simulation with $N^2 = 1024^2$.

The significance of the symmetric square root method for FENE-P is much more apparent in terms of stability. The fact is that we can increase Wi much more than we can for Stokes–Oldroyd-B. We show results from two different simulations to demonstrate this. First in Fig. 5 (c) and (d) we show results from perturbed initial data with Wi = 20 at t = 100, with l^2 = 225. This is just after

the onset of the instability and the flow is still nearly symmetric. The stress has accumulated along the incoming and outgoing streamlines of the extensional stagnation point and the four-roll mill structure of the vorticity is still largely preserved. Fig. 5 (e) and (f) shows results from perturbed initial data with Wi = 50 at t = 500, with l^2 = 225. These same computations evolving $\mathbf{c}$ fail to produce finite values before t = 60 whereas the evolution of $\mathbf{b}$ appears to continue indefinitely—although, again, there must be some loss of accuracy. The qualitative behavior is similar to the solutions of Stokes–Oldroyd-B and the instabilities discussed for that case also occur here. In Fig. 5 (c) and (e) we show contour plots of tr($\mathbf{S}(\mathbf{b}^2)$) after the instabilities have developed and observe that max tr($\mathbf{S}$) is quite large. The time-dependent behavior is also quite complicated and as one can see in Fig. 5 (f), the vorticity of the flow is also very complex with many additional vortices continually arising and being destroyed in the flow.

4. Discussion and conclusions

In hindsight both the symmetrization procedure and the direct computation of the square root evolution Eqs. (9) and (10) might have been expected to contribute to the gains in stability and accuracy. Taking the square root reduces large amplitudes which, not unexpectedly, reduces the stiffness in time stepping.[2] Moreover symmetrizing the system may reduce the stiffness of the time marching as compared to taking $\mathbf{a} = \mathbf{0}$ and simply computing the deformation tensor because components of the symmetric square root matrix will generally have less variance than a square root with no symmetry. And computing the square root instead of $\mathbf{c}$ has other advantages: the square root computation ensures positivity of $\mathbf{c}$ in the numerical scheme compared to the most direct evolution of the conformation tensor. We have observed that in practice the square root method can be applied at higher Wi and for longer time without any artificial numerical stress diffusion than evolving the

---

[2] Clearly, the positive $(2k)th$-roots of $\mathbf{c}$ have entries with even smaller amplitude compared to $\mathbf{c}$ when stress gets very large, which may help the numerics. This advantage is most aggressively pursued in methods where one computes the logarithm of the matrix $\mathbf{c}$ but these methods can be computationally expensive and more complicated to implement [1]. A comparison of the square-root method with the logarithm method [1] and the method of evolving eigenvalues [2] is planned for a future study.
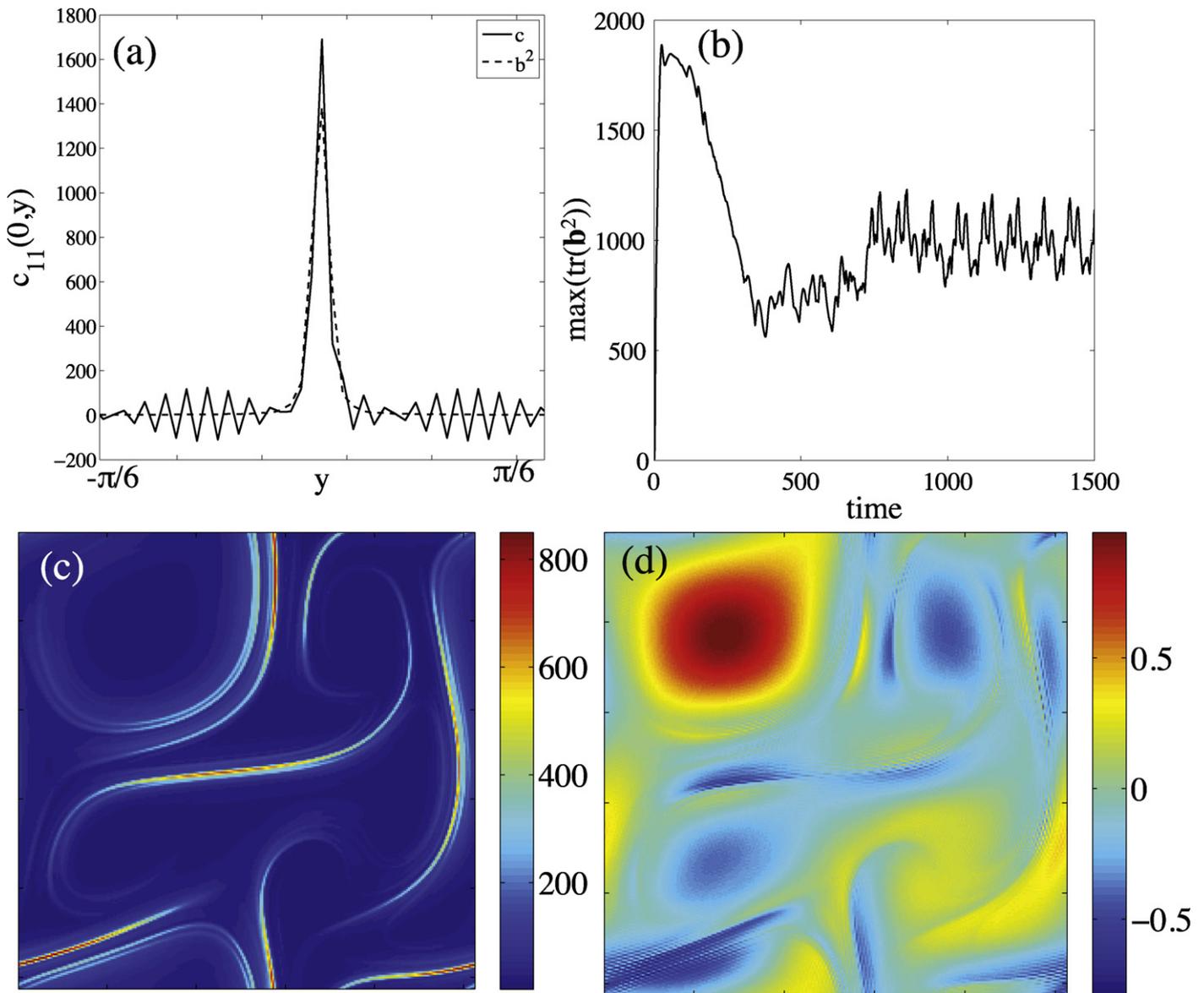
Fig. 4. (a) Plot of first component of conformation tensor $c_{11}(0, y)$ and $b_{11}^2(0, y)$ along direction of compression near the extensional stagnation point for Wi = 10 at $t = 15$. Computations of $\mathbf{c}$ stop producing finite values at $t = 19$. (b) Plot of max(tr($\mathbf{b}^2$)) as a function of time over $0 < t < 1500$. (c) Wi = 10, contour plot of tr($\mathbf{b}^2$) at $t = 1000$ on $[-\pi, \pi]^2$. (d) Wi = 10, contour plot of the vorticity of the flow field at $t = 1000$ on $[-\pi, -\pi]^2$. All simulations performed with $N^2 = 256^2$ grid points.

conformation tensor directly can, enabling one to obtain numerical solutions in more situations.

One less obvious but perhaps important advantage is the following. Assuming the locality of modal interactions, i.e., that lower spectral modes of $\mathbf{c}$ are determined predominantly by lower modes of the square root matrix $\mathbf{b}$, we can expect good information about up to the first $2N$ modes of the conformation tensor $\mathbf{c}$ when we know just the first N modes of the square root $\mathbf{b}$. This speculation basically boils down to the assumption that the Galerkin approximation method works well for both $\mathbf{b}$ and $\mathbf{c}$ for sufficiently large N. Thus we might expect that evolution of the square root improves both stability and accuracy, at least in spectral or pseudospectral schemes. Whether this is the case in other types of spatial discretizations requires further investigation. Of course it also remains to implement the full $n = 3$ dimensional symmetric square root algorithm and systematically compare its performance with conventional

schemes used to investigate, for example, turbulent drag reduction [20].

We emphasize that all the numerical simulations shown have been performed without artificial diffusion. The form of the equations with added stress diffusion is given in Appendix B. The square-root method still has limitations for sufficiently large Wi so it is natural to ask if one could use a more physically realistic diffusion coefficient with the square-root method and this will be pursued in future work.

The advantage of expressing the Oldroyd-B and FENE-P models as evolutions in a vector space (indeed, a Hilbert space) remains one of theoretical elegance at this point. Whether or not this formulation might assist the rigorous mathematical analysis of these models is an open question. Nevertheless it opens up new possibilities including the development of energy stability methods and the implementation of diagnostic tools like proper orthogonal decomposition [21] for the polymer configuration field.
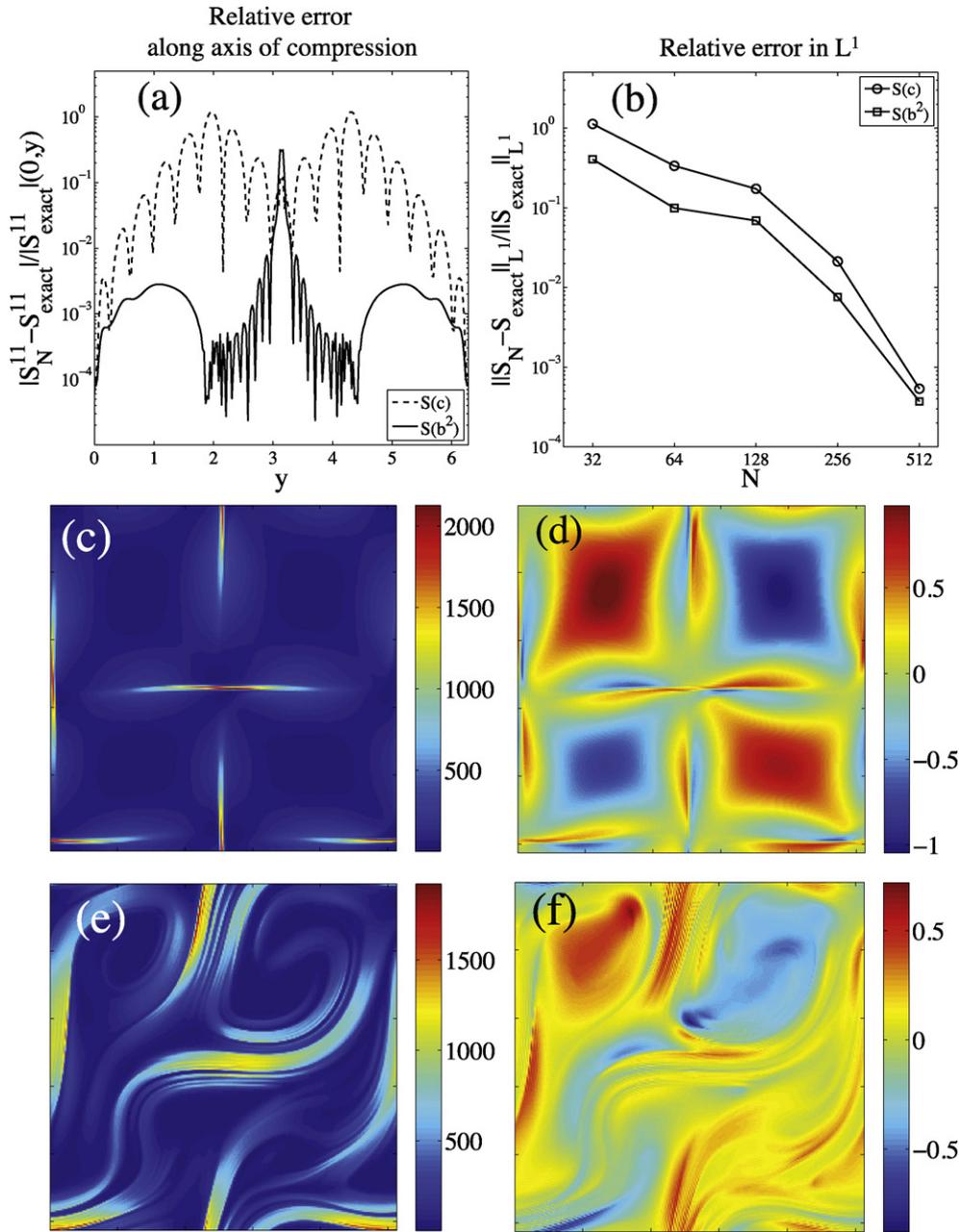
Fig. 5. (a) Relative error $|\mathbf{S}_N - \mathbf{S}_{\mathrm{exact}}|/|\mathbf{S}_{\mathrm{exact}}|$ measured along the axis of compression of the first component of $\mathbf{S}(\mathbf{c})$ for FENE-P with $N^2 = 256^2$, Wi = 5 at $t = 10$, $l^2 = 100$. Dotted line is $\mathbf{S}(\mathbf{c})$ and solid line is $\mathbf{S}(\mathbf{b}^2)$. (b) Relative error in L^1 shows $\|\mathbf{S}_N - \mathbf{S}_{\mathrm{exact}}\|_{L^1}/\|\mathbf{S}_{\mathrm{exact}}\|_{L^1}$ computed with $\mathbf{S}(\mathbf{c})$ and $\mathbf{S}(\mathbf{b}^2)$, for Wi = 5 at $t = 10$, $l^2 = 100$. (c) Wi = 20, contour plot of $\mathrm{tr}(\mathbf{S}(\mathbf{b}^2))$ at $t = 100$ on $[-\pi, \pi]^2$, $l^2 = 225$. (d) Wi = 20, contour plot of the vorticity of the flow field at $t = 100$ on $[-\pi, -\pi]^2$, $l^2 = 225$. All simulations done with $N^2 = 256^2$ grid points. (e) Wi = 50, contour plot of $\mathrm{tr}(\mathbf{S}(\mathbf{b}^2))$ at $t = 500$ on $[-\pi, \pi]^2$, $l^2 = 225$. (f) Wi = 50, contour plot of the vorticity of the flow field at $t = 500$ on $[-\pi, -\pi]^2$, $l^2 = 225$. All simulations done with $N^2 = 256^2$ grid points.

Acknowledgements

Appendix A. Entries of the antisymmetric matrix for n = 3

The entries a_{12}, a_{13}, a_{23} of the antisymmetric matrix **a** in (11) are given by

$$D a_{12} = \left(T_1 T_2 - B_3^2\right) w_1 - (B_1 T_1 + B_3 B_2) w_2 + (B_2 T_2 + B_1 B_3) w_3, \quad (32)$$

$$D a_{13} = -(B_1 T_1 + B_3 B_2) w_1 + \left(T_1 T_3 - B_2^2\right) w_2 - (B_2 B_1 + B_3 T_3) w_3, \quad (33)$$

$$D a_{23} = (B_2 T_2 + B_1 B_3) w_1 - (B_2 B_1 + B_3 T_3) w_2 + \left(T_2 T_3 - B_1^2\right) w_3, (34)$$

where

$$
\begin{aligned}
D &\equiv \det((\mathrm{tr}\,\mathbf{b})\mathbf{I} - \mathbf{b}) \\
&= T_1 \left(T_2 T_3 - B_1^2\right) - B_2 (B_2 T_2 + B_1 B_3) - B_3 (B_2 B_1 + B_3 T_3),
\end{aligned} \quad (35)
$$

$$T_1 = b_{22} + b_{33}, \quad T_2 = b_{11} + b_{33}, \quad T_3 = b_{11} + b_{22}, \quad (36)$$

$$B_3 = b_{12}, \quad B_2 = b_{13}, \quad B_1 = b_{23}, \quad (37)$$

and w_1, w_2, and w_3 are given in (17)–(19).

Appendix B. Stress diffusion

To include stress diffusion in the dynamics of **b**, note that

$$\partial_{xx} c_{ij} = \partial_{xx}(b_{ik}b_{jk}) = b_{ik}(\partial_{xx}b_{jk}) + (\partial_{xx}b_{ik})b_{jk} + 2\partial_x b_{ik}\partial_x b_{jk},$$

and similarly for y and z. In matrix notation,

$$\Delta \mathbf{c} = (\Delta \mathbf{b})\mathbf{b} + \mathbf{b}(\Delta \mathbf{b}) + 2\left[(\partial_x \mathbf{b})^2 + (\partial_y \mathbf{b})^2 + (\partial_z \mathbf{b})^2\right].$$

Denoting the stress diffusion coefficient by ζ, the term

$$\zeta\left(\frac{1}{2}\Delta \mathbf{b} + \mathbf{h}\right),$$

where

$$\mathbf{h} = \mathbf{b}^{-1}\left[\frac{1}{2}(\Delta \mathbf{b})\mathbf{b} + (\partial_x \mathbf{b})^2 + (\partial_y \mathbf{b})^2 + (\partial_z \mathbf{b})^2\right],$$

is then added to the right hand side of the evolution equation for **b** (i.e., (9) or (10)) to produce the effect of a $\zeta\Delta\mathbf{c}$ term in the conformation tensor equation. In case of the Oldroyd-B the equation beomes

$$\left(\frac{\partial}{\partial t} + \mathbf{u}\cdot\nabla\right)\mathbf{b} = \zeta\left(\frac{1}{2}\Delta\mathbf{b} + \mathbf{h}\right) + \mathbf{b}\nabla\mathbf{u} + \mathbf{ab} + \frac{1}{2\mathrm{Wi}}\left(\mathbf{b}^{-1} - \mathbf{b}\right)$$

$$= \frac{\zeta}{2}\Delta\mathbf{b} + \frac{1}{2\mathrm{Wi}}\left(\mathbf{b}^{-1} - \mathbf{b}\right) + \zeta\mathbf{h} + \mathbf{b}\nabla\mathbf{u} + \mathbf{ab}$$

and to symmetrize the equation, instead of defining **r** as in (13), we set

$$\mathbf{r} = (r_{ij}) = \zeta\mathbf{h} + \mathbf{b}\nabla\mathbf{u} + \mathbf{ab}.$$

This does not affect the solvability of **a**. It only changes the definition of w_1, w_2, w_3. With this choice, the diffusion term in the **b** equation takes the form $\zeta/(2\Delta\mathbf{b})$, where ζ is the diffusion constant in the conformation tensor equation. The antisymmetric matrix **a** is computed with modified w_1, w_2, w_3. More precisely, let us introduce the notation

$$\partial_{x_m}\mathbf{b} = (b_{ij,m}), \quad i, j, m = 1, 2, 3,$$
$$\Delta\mathbf{b} = (\Delta b_{ij}), \quad i, j = 1, 2, 3,$$
$$\mathbf{b}^{-1} = (\pi_{ij}), \quad i, j = 1, 2, 3,$$

where

$$
\begin{aligned}
B\pi_{11} &= b_{22}b_{33} - b_{23}^2,\\
B\pi_{12} &= b_{13}b_{23} - b_{12}b_{33},\\
B\pi_{13} &= b_{12}b_{23} - b_{13}b_{22},\\
B\pi_{22} &= b_{11}b_{33} - b_{13}^2,\\
B\pi_{23} &= b_{12}b_{13} - b_{11}b_{23},\\
B\pi_{33} &= b_{11}b_{22} - b_{12}^2,\\
B &= \det(\mathbf{b})\\
&= b_{11}\left(b_{22}b_{33} - b_{23}^2\right) + b_{12}\left(b_{13}b_{23} - b_{12}b_{33}\right)\\
&\quad + b_{13}\left(b_{12}b_{23} - b_{13}b_{22}\right),
\end{aligned}
$$

and the other entries are determined by symmetry of $\mathbf{b}^{-1}$. Then, we change w_1, w_2, w_3 as follows. Let W_1, W_2, W_3 denote the new values for the system with diffusion, and w_1, w_2, w_3 denote the old values for the equations without diffusion. Then,

$$
\begin{aligned}
W_1 &= w_1 + \frac{\zeta}{2}\left(\pi_{2k}\Delta b_{ki}b_{i1} - \pi_{1k}\Delta b_{ki}b_{i2}\right)\\
&\quad + \zeta\left(\pi_{2k}b_{ki,m}b_{i1,m} - \pi_{1k}b_{ki,m}b_{i2,m}\right),\\
W_2 &= w_2 + \frac{\zeta}{2}\left(\pi_{3k}\Delta b_{ki}b_{i1} - \pi_{1k}\Delta b_{ki}b_{i3}\right)\\
&\quad + \zeta\left(\pi_{3k}b_{ki,m}b_{i1,m} - \pi_{1k}b_{ki,m}b_{i3,m}\right),\\
W_3 &= w_3 + \frac{\zeta}{2}\left(\pi_{3k}\Delta b_{ki}b_{i2} - \pi_{2k}\Delta b_{ki}b_{i3}\right)\\
&\quad + \zeta\left(\pi_{3k}b_{ki,m}b_{i2,m} - \pi_{2k}b_{ki,m}b_{i3,m}\right),
\end{aligned}
$$

where we sum over repeated indices $i, k, m = 1, 2, 3$ in 3D, and $i, k, m = 1, 2$ in 2D (where only w_1 and W_1 are present).

In particular, in 2D, (27) becomes

$$a_{12} = \frac{\left(b_{12}u_{1,1} - b_{11}u_{2,1}\right) + \left(b_{22}u_{1,2} - b_{12}u_{2,2}\right) + A}{b_{11} + b_{22}}, \tag{38}$$

where

$$A = \frac{\zeta}{2}\left(\pi_{2k}\Delta b_{ki}b_{i1} - \pi_{1k}\Delta b_{ki}b_{i2}\right) + \zeta\left(\pi_{2k}b_{ki,m}b_{i1,m} - \pi_{1k}b_{ki,m}b_{i2,m}\right),$$
$$i, k, m = 1, 2.$$

Thus, we change the evolution Eq. (9) for **b** to

$$\left(\frac{\partial}{\partial t} + \mathbf{u}\cdot\nabla - \frac{\zeta}{2}\Delta\right)\mathbf{b} = \frac{1}{2\mathrm{Wi}}\left(\mathbf{b}^{-1} - \mathbf{b}\right) + \mathbf{b}\nabla\mathbf{u} + \mathbf{ab} + \zeta\mathbf{h}, \tag{39}$$

and compute a_{12} as in (38).

All that being said, we remark that if stress diffusion is included for computational purposes, i.e., to numerically stabilize and/or regularize particular calculations, it may be just as effective to simply add a term $\sim\Delta\mathbf{b}$ to the square root's evolution Eq. (9) or (10).

Appendix C. Supplementary Data

Supplementary data associated with this article can be found, in the online version, at doi:10.1016/j.jnnfm.2011.02.008.

References

[1] R. Fattal, R. Kupferman, Time-dependent simulation of viscoelastic flows at high weissenberg number using the log-conformation representation, J. Non-Newtonian Fluid Mech. 126 (1) (2005) 23–37.

[2] T. Vaithianathan, A. Robert, J.G. Brasseur, L.R. Collins, An improved algorithm for simulating three-dimensional, viscoelastic turbulence, J. Non-Newtonian Fluid Mech. 140 (1–3) (2006) 3–22 (Special Issue on the XIVth International Workshop on Numerical Methods for Non-Newtonian Flows, Santa Fe, 2005, XIVth International Workshop on Numerical Methods for Non-Newtonian Flows, Santa Fe, 2005).

[3] A. Lozinski, R.G. Owens, An energy estimate for the Oldroyd B model: theory and applications, J. Non-Newtonian Fluid Mech. 112 (2–3) (2003) 161–176.

[4] C.R. Doering, B. Eckhardt, J. Schumacher, Failure of energy stability in Oldroyd-B fluids at arbitrarily low Reynolds numbers, J. Non-Newtonian Fluid Mech. 135 (2006) 92–96.

[5] B. Thomases, M. Shelley, Emergence of singular structures in Oldroyd-B fluids, Phys. Fluids 19 (2007) 103103.

[6] B. Thomases, M. Shelley, Transition to mixing and oscillations in a Stokesian viscoelastic flow, Phys. Rev. Lett. 103 (2009) 094501.

[7] M. Renardy, A comment on smoothness of viscoelastic stresses, J. Non-Newtonian Fluid Mech. 138 (2006) 204–205.

[8] J.M. Rallison, E.J. Hinch, Do we understand the physics in the constitutive equation? J. Non-Newtonian Fluid Mech. 29 (1988) 37–55.

[9] A.W. El-Kareh, L.G. Leal, Existence of solutions for all Deborah numbers for a non-Newtonian model modified to include diffusion, J. Non-Newtonian Fluid Mech. 33 (1989) 257.

[10] R. Peyret, Spectral Methods for Incompressible Viscous Flow, Springer, New York, 2002.

[11] T.Y. Hou, R. Li, Computing nearly singular solutions using pseudo-spectral methods, J. Comput. Phys. 226 (2007) 379–397.

[12] B. Thomases, M. Shelley, J.-L. Thiffeault, A Stokesian viscoelastic flow: transition to mixing and oscillations. In preparation, 2010.

[13] A. Groisman, V. Steinberg, Elastic turbulence in a polymer solution flow, Nature 405 (2000) 53–55.

[14] A. Groisman, V. Steinberg, Efficient mixing at low Reynolds numbers using polymer additives, Nature 410 (2001) 905–908.

[15] A. Groisman, V. Steinberg, Elastic turbulence in curvilinear flows of polymer solutions, New J. Phys. 4 (2004) 74437–74447.

[16] P.E. Arratia, C.C. Thomas, J. Diorio, J.P. Gollub, Elastic instabilities of polymer solutions in cross-channel flow, Phys. Rev. Lett. 96 (2006) 144502.

[17] R.J. Poole, M.A. Alves, P.J. Oliveira, Purely elastic flow asymmetries, Phys. Rev. Lett. 99 (2007) 164503.

[18] S. Berti, A. Bistagnino, G. Boffetta, A. Celani, S. Musacchio, Two-dimensional elastic turbulence, Phys. Rev. E 77 (2008) 055306.

[19] L. Xi, M.D. Graham, A mechanism for oscillatory instability in viscoelastic cross-slot flow, J. Fluid Mech. 622 (-1) (2009) 145–165.

[20] L. Xi, M.D. Graham, Turbulent drag reduction and multistage transitions in viscoelastic minimal flow units, J. Fluid Mech. 647 (2010) 421–452.

[21] H.-N. Zhang, X.-B. Li, B. Yu, J.-J. Wei, Y. Kawaguchi, W.-H. Cai, F.-C. Li, K. Hishida, Study on the characteristics of turbulent drag-reducing channel flow by particle image velocimetry combining with proper orthogonal decomposition analysis, Phys. Fluids 21 (2009) 115103.